Chemical Engineering Journal 545 (2026) 179515

Contents lists available at ScienceDirect

Chemical Engineering Journal

journal homepage: www.elsevier.com/locate/cej

Continuous struvite production from liquid sidestream digestate using a planar oscillatory flow crystallizer: Kinetic analysis and process assessment

Luiza Sena [a,b], Catarina Cruzeiro [a], António Ferreira [b], Vítor J.P. Vilar [a,*]

[a] LSRE-LCM, ALiCE, Faculty of Engineering, University of Porto, Rua Dr. Roberto Frias, 4200-465, Porto, Portugal
[b] LEPABE, ALiCE, Faculty of Engineering, University of Porto, Rua Dr. Roberto Frias, 4200-465, Porto, Portugal

ARTICLE INFO

Keywords:
Struvite
Sidestream digestate
Phosphorus recovery
Oscillatory flow reactor
Nutrient recovery

ABSTRACT

The recovery of phosphorus and nitrogen from municipal wastewater is receiving growing attention across Europe as a strategy to reduce dependence on conventional fertilizers and advance circular nutrient management. In this context, several full-scale systems have been implemented at wastewater treatment plants (WWTPs) to recover nutrients from liquid sidestream digestate (SD), a by-product of anaerobic digestion. In this study, a planar Oscillatory Flow Crystallizer (planar-OFC) was evaluated as an alternative approach for the continuous recovery of nutrients as struvite, a slow-release fertilizer, from SD. The influence of key operational parameters, including hydraulic retention time, reagent dosage, temperature, and pH, was systematically assessed under both batch and continuous modes. In parallel, thermodynamic analyses were conducted to better understand struvite solubility and ionic equilibria in SD matrices. Under the best conditions identified in this study, phosphorus recovery exceeded 80%, with a maximum struvite production of 1.1 kg/m^3. The kinetics of phosphate recovery were well described by a pseudo-first-order model within the investigated operating conditions, with rate constants above 14 h^{-1}. Thermodynamic results further identified a favorable temperature range for struvite crystallization. The recovered solids were confirmed to consist predominantly of struvite as the main crystalline phase, with overall chemical purities of at least 92%. Overall, the results demonstrate that the planar-OFC is an effective and compact technology for nutrient recovery, capable of producing high-quality struvite despite the complex composition of SD streams. The findings also validate the proposed kinetic model and highlight the robustness of the reactor design for practical applications.

1. Introduction

According to the International Fertilizer Association (IFA), between 1963 and 2023, global demand for phosphorus pentoxide (P_2O_5) and nitrogen (N) used as fertilizers increased steadily at average annual rates of 6% and 13%, respectively [1]. However, this increased demand, coupled with the intermittent and limited natural availability of phosphorus (P), the high production costs of N-based chemicals, and recent geopolitical conflicts and market instability, has intensified the need for local and independent nutrient sources, particularly in Europe. Consequently, alternative routes for fertilizer production have been explored to promote more accessible agriculture, reduce dependence on imports, and ensure food security [2,3]. The recovery of nutrients (P and N) from waste-derived streams has emerged as a sustainable strategy to close nutrient cycles and supplement conventional fertilizer sources. Sidestream digestate (SD), a liquid by-product of anaerobic digestion, represents a suitable source for nutrient recovery due to its high N and P content [4]. These characteristics favor the formation of struvite ($MgNH_4PO_4{\cdot}6H_2O$), a mineral that often precipitates unintentionally in wastewater treatment plants (WWTPs), increasing maintenance costs and causing problems such as pipe scaling and clogging. However, when precipitation is controlled within a reactor, struvite can be harvested and used as a slow-release fertilizer [2,5]. Struvite production is a well-established method for nutrient recovery from SD, with several full-scale technologies implemented at WWTPs, including NuReSys®, ANPHOS®, Airprex®, and Pearl®. Nevertheless, these systems rely on continuously stirred tank reactors (CSTR) or fluidized bed reactors, which can present disadvantages, such as mass and heat transfer limitations, broad residence time distribution, scale-up issues, and high energy and maintenance requirements [6–9].

To overcome these drawbacks, the present work explored the use of a planar oscillatory flow crystallizer (OFC), a variant of a plug flow

* Corresponding author.
E-mail address: vilar@fe.up.pt (V.J.P. Vilar).

https://doi.org/10.1016/j.cej.2026.179515
Received 15 May 2026; Received in revised form 11 July 2026; Accepted 13 July 2026
Available online 14 July 2026
1385-8947/© 2026 The Authors. Published by Elsevier B.V. This is an open access article under the CC BY-NC license (http://creativecommons.org/licenses/by-nc/4.0/).

crystallizer (PFC), which improves the suspension and transportation of solids. One of the OFC's major benefits is its ability to operate in continuous flow at low net flow rates while maintaining good mixing and plug-flow behavior, and allowing scale-up prediction [10,11]. The OFC systems have been used for crystallization processes to produce high-value chemicals, such as antibodies, proteins, and active pharmaceutical ingredients [12,13], [14–19].

In this work, a novel application of continuous reactive crystallization was performed in a planar-OFC to produce struvite, a slow-release fertilizer, from SD. The kinetics of the crystallization process using the lab-scale prototype were elucidated both in batch and continuous mode using a real SD liquor, and operational parameters, such as pH, temperature, feeding scheme, reactants dosage, and ionic composition of SD samples, were investigated to evaluate their impact on the rate of struvite formation and phosphorus recovery.

2. Materials and methods

2.1. Collection and characterization of sidestream digestate

SD samples, obtained by centrifugation of the anaerobic digester residue (digestate), were collected at two municipal WWTPs from Northern Portugal. The sample designated "WW1" was used to develop the kinetic model. Two additional SD samples, denoted "WW2" and "WW3", were collected in different months to account for seasonal variations in ionic composition and were used to validate the kinetic model. After collection, the samples were divided into equal portions and frozen to minimize their degradation. Before each experiment, samples were unfrozen and kept in a fridge at 4 °C. The pH and inorganic ion concentrations were routinely monitored to ensure the stability of the SD characteristics. The chemical characterization of all samples is presented in Table 1, and the detailed instrumental and analytical procedures are described in Section S1 of the Supplementary material.

Table 1
Chemical characteristics of the sidestream digestate samples obtained from Portuguese municipal WWTPs. Values represent the mean of triplicate analyses. * indicates the limit of quantification (LOQ) of the analytical method.

	Kinetic study	Validation of the kinetic model	
	WW1	WW2	WW3
	Values (av ± SD)		
Parameter (units)			
pH at 25 °C	7.7 (±0.1)	7.8 (±0.1)	7.9 (±0.2)
Temperature (°C)	20.5 (±0.1)	24.1 (±0.3)	21.5 (±0.1)
Conductivity (mS/cm)	4.4 (±0.1)	3.3 (±0.1)	5.4 (±0.1)
Dissolved organic carbon (mg/L)	56 (±2)	18.9 (±0.8)	14.8 (±0.2)
Dissolved inorganic carbon (mg/L)	87 (±2)	268 (±1)	431 (±2)
Chemical oxygen demand (mg O_2/L)	227 (±4)	158 (±6)	113 (±4)
Total suspended solids (mg/L)	597 (±13)	45 (±2)	128 (±2)
Volatile suspended solids (mg/L)	428 (±17)	32 (±1)	107 (±5)
Fixed solids (mg/L)	169 (±12)	13 (±2)	21 (±1)
Inorganic ions			
Chloride – Cl^- (mg/L)	312 (±3)	91.4 (±0.2)	114.6 (±0.5)
Nitrite – NO_2^- (mg/L)	31.1 (±0.4)	161.3 (±0.4)	35.1 (±0.1)
Nitrate – NO_3^- (mg/L)	0.48 (±0.01)	153 (±1)	6.6 (±0.7)
Ammonium – NH_4^+ (mg/L)	492 (±1)	239 (±1)	675 (±5)
Sulphate – SO_4^{2-} (mg/L)	47 (±1)	58.5 (±0.4)	105 (±1)
Bromide – Br^- (mg/L)	1.10 (±0.01)	<0.01*	2.1 (±0.1)
Phosphate – PO_4^{3-} (mg/L)	173.1 (±0.7)	169.6 (±0.6)	445 (±3)
Calcium – Ca^{2+} (mg/L)	41 (±3)	12.5 (±0.3)	53 (±5)
Magnesium – Mg^{2+} (mg/L)	6.0 (±0.1)	17.2 (±0.8)	3.0 (±0.4)
Potassium – K^+ (mg/L)	123 (±1)	85 (±2)	179 (±2)
Sodium – Na^+ (mg/L)	216 (±2)	67.4 (±0.6)	77 (±1)

2.2. Kinetics studies of the crystallization process

A kinetic study was performed to clarify how operational conditions govern the progression of struvite formation over time and influence phosphorus recovery from SD. Knowledge of nucleation and crystal growth rates enables the identification of factors controlling precipitation efficiency and optimization of process conditions. Batch and continuous experiments were conducted using WW1. Preliminary studies demonstrated that suspended solids present in the SD significantly affected both the purity of the recovered struvite and the reproducibility of the crystallization experiments. Precisely, particulate and organic matter promoted heterogeneous nucleation and co-precipitation phenomena, leading to variability in experimental outcomes and the formation of impure solids. Moreover, as illustrated in Fig. S1, unfiltered samples produced a heterogeneous brown solid consisting of crystalline material mixed with organic matter, whereas filtered samples yielded a white solid. This observation reinforces that suspended solids in unfiltered samples contaminate the product and reduce its purity. Therefore, all SD samples were subjected to an additional filtration step using qualitative filter paper (particle retention of 5–13 μm) before the crystallization experiments. This pre-treatment step was implemented to reduce the influence of suspended solids, improve experimental consistency, and enable a more controlled evaluation of crystallization kinetics. The recovery efficiency of P, N, and Mg, R (%), was obtained by Eq. (1), where C_t and C_0 are the concentrations (mg PO_4^{3-}/L; mg NH_4^+/L; mg Mg^{2+}/L) at time t and time 0 (initial), respectively [20].

$$R\ (\%) = \left(1 - \frac{C_t}{C_0}\right) \times 100 \quad (1)$$

2.2.1. Batch crystallization experiments

Batch experiments were performed to: i) understand the mechanisms of struvite generation; ii) assess induction times of struvite's crystallization; iii) determine struvite's solubility. The schematic experimental setup used in batch crystallization is shown in Fig. S2. A 250 mL sample was placed in a double-walled Pyrex glass vessel, thermostated via water circulation from a constant-temperature bath (Ministat 125, Huber), and stirred mechanically at 300 rpm (RSM-02-HP, Phoenix) using a Teflon-coated stirring bar. The pH and temperature were maintained constant. A solution of 0.23 M NaOH (98.5% purity, Thermo Scientific, CAS # 1310-73-2) was used to adjust the pH of the reaction medium. For magnesium supply, a solution of 97.9 mM $MgCl_2$ (>98% purity, anhydrous, Thermo Scientific, CAS # 7786-30-3) was used. The kinetics of struvite crystallization were assessed at a final pH = 9, and the experimental conditions tested are presented in Table 2. The online measurement of magnesium concentration was conducted with a mini Mg^{2+} ion-selective electrode (ISE, NT Sensors, Imacimus 2, S/N: C3X7–12), and the calibration curve of the sensor is presented in Fig. S3.

The induction time was determined from the pH vs time curves using the tangent method. For each Mg:P molar ratio, tangent lines were drawn at two regions: the initial plateau where the pH remained stable after NaOH addition, and the onset of pH decline, which marked the beginning of struvite nucleation. The intersection point of these lines was taken as τ_{ind}. This approach provided a precise estimation of the time required for nucleation [21,22].

2.2.2. Continuous crystallization experiments

Based on outputs from batch experiments, the crystallization process was scaled up to a continuous configuration using the planar-OFC to validate performance at the lab scale. The experimental setup for the continuous crystallization process is presented in Fig. 1, and further details regarding the reactant dosing configuration and the planar-OFC description are provided in Sections S2 and S3 (Supplementary

Table 2
Summary of the experimental conditions (batch and continuous mode using the planar-OFC) investigated for the kinetics of struvite crystallization. All trials were conducted at $[PO_4^{3-}]_{Initial} = 1.82$ mM and $[NH_4^+]_{Initial} = 27.3$ mM. Experiments were run in triplicate.

Mode	pH_{Final}	Q_W (mL/min)	Initial Mg:P molar ratio	Temperature (°C)
Batch	9.0	–	1.3	20
	9.0	–	1.4	20
	9.0	–	1.5	20
	9.0	–	1.6	10, 15, 20, 30, 40
Continuous (Planar-OFC)	9.0	16, 23, 55, and 63	1.3	20
	9.0	16, 23, 55, and 63	1.4	20
	9.0	16, 23, 55, and 63	1.5	20
	9.0	16, 23, 55, and 63	1.6	10, 15, 20, 30, 40
	9.5	16	1.3, 1.4, 1.5, 1.6	20

material). To evaluate the kinetics of continuous struvite production at the planar-OFC, a wide range of experimental conditions was investigated, as summarized in Table 2.

To test the robustness of the obtained kinetic model and assess the effect of ionic composition, the continuous crystallization process in a planar OFC was applied under the most favorable conditions identified to two additional SD samples (WW2 and WW3). The recovery percentages of magnesium, phosphorus, and nitrogen were evaluated, along with the morphology and purity of the solid formed.

2.3. Solid analyses

The morphology of the solids harvested at the outlet of the planar-OFC immediately after the crystallization process was analyzed through stereoscopic microscopy (Zeiss Standard 20 microscope) at 10× and 40× magnification. For physical characterization, the filtered solids were dried at 40 °C for 48 h to prevent ammonia (NH_3) loss through volatilization. Once it reached a constant weight, the solid was stored in a desiccator. Further details on the physical characterization are provided in the Supplementary material.

3. Results and discussion

3.1. Struvite crystallization: process overview

Struvite is a white crystalline solid formed by magnesium, phosphate, and ammonium, as shown in Eq. (2). An overview of reported studies (Table S1) illustrates how different operational conditions, reactor types, and reagent strategies influence phosphorus recovery as struvite and crystal characteristics. This comparison highlights the broad variability in initial phosphate concentrations, pH control, magnesium dosing, and residence times, reflecting the lack of a standardized approach and underscoring the importance of understanding how each parameter affects the crystallization process.

$$Mg^{2+}{}_{(aq)} + NH_4{}^{+}{}_{(aq)} + H_2PO_4{}^{-}{}_{(aq)} + 6H_2O_{(l)} \rightarrow MgNH_4PO_4 \bullet 6H_2O_{(s)} + 2H^{+}{}_{(aq)} \quad (2)$$

Several factors influence struvite precipitation, including the molar ratios of the reagents, the quantity and type of chemicals added, pH, temperature, reactor type, and operational mode (batch or continuous). These parameters influence P and N recoveries and can affect crystal nucleation and growth rates, thereby altering particle morphology and size [23]. For this reason, understanding how each parameter influences the struvite precipitation process is essential. Careful evaluation and control of these conditions are crucial to optimize crystal formation, maximize nutrient recovery, and ensure both high process efficiency and economic viability.

3.2. Parametric analysis of crystallization parameters in batch mode

Batch crystallization experiments were conducted as a preliminary step to support the design and analysis of key variables governing the continuous crystallization process at the planar-OFC. Specifically, batch mode enabled evaluation of NaOH dosing requirements, determination of the induction time for struvite nucleation, assessment of equilibrium phosphate concentrations at different initial Mg:P molar ratios, and plotting of the struvite solubility curve as a function of temperature.

3.2.1. Sodium hydroxide dosing and final pH

The pH was monitored upon the addition of 0.23 M NaOH to determine the required dose to reach the target pH. It was observed that increasing the Mg:P molar ratio did not alter the required NaOH dosage, as phosphate was the limiting reactant. This condition was characterized by an excess of NH_4^+, limited PO_4^{3-} availability, and Mg^{2+} dosed in

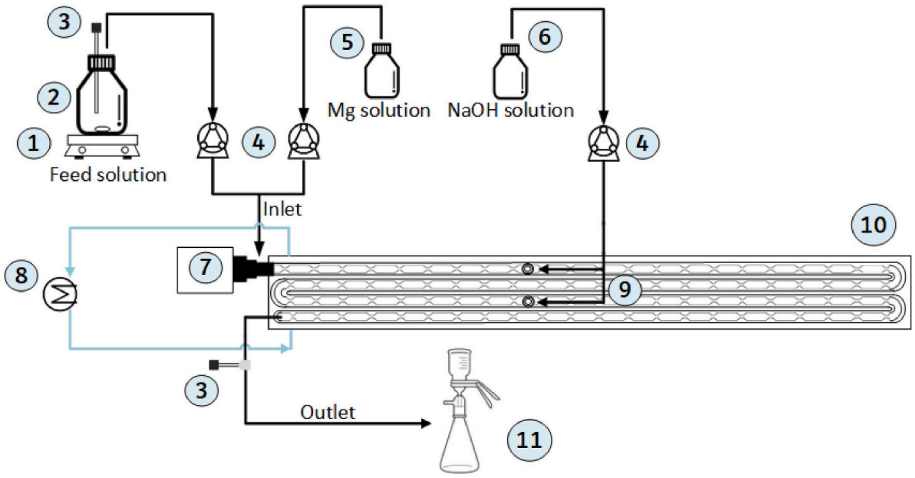


Fig. 1. Experimental setup for continuous struvite crystallization. 1 – Magnetic stirrer and magnetic bar; 2 – Sidestream digestate (feed solution); 3 – Thermometer; 4 – Peristaltic pump; 5 – $MgCl_2$ solution; 6 – NaOH solution; 7 – Linear motor; 8 – Thermostatic bath for heat exchange; 9 – Intermediate injection points; 10 – Planar-OFC; 11 – Vacuum filtration system.

proportion to the initial phosphate concentration.

A volume of 1 mL of NaOH solution was added to 250 mL of side-stream digestate in a thermostated glass vessel (T = 20 °C) at 1-minute intervals until the pH reached approximately 9.5, corresponding to the region of lower struvite solubility [24]. Despite the different ionic composition, the behavior of magnesium recoveries ($R_{Mg^{2+}}$) for all the samples (WW1 to WW3) exhibited a similar sigmoidal (S-shaped) trend (Fig. 2).

Initially, recovery changed minimally, indicating a low reaction rate. After the addition of a certain amount of NaOH, recovery increased sharply, and the formation of a solid was visually detected. This corresponded to the onset of nucleation and crystal growth, when supersaturation was high, and conditions became favorable for struvite formation. The inflection point, highlighted in Fig. 2, corresponded to the pH at which struvite nucleated under the given conditions, ranging from ≈ 8.3 (WW1 and WW3) to ≈ 8.6 (WW2). The plateau marked the point at which the curve levels off, indicating that equilibrium had been achieved. Since WW2 contained two to three times less NH_4^+ (Table 1) than WW1 and WW3, a higher supersaturation had to be reached by increasing the pH, resulting in a greater NaOH requirement to trigger nucleation compared to WW1 and WW3 [25].

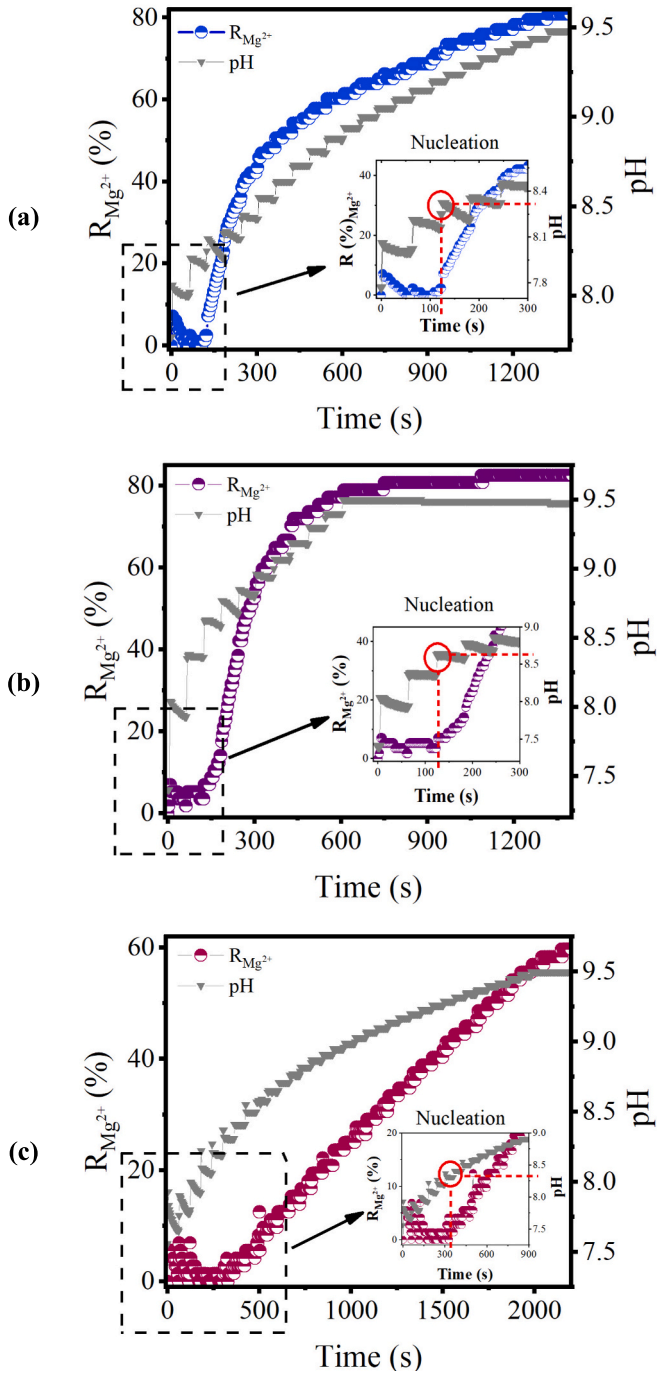


Fig. 2. Variation of magnesium recovery, $R_{Mg^{2+}}$(%), as a function of time and pH for (a) WW1 (blue), (b) WW2 (purple), and (c) WW3 (magenta) samples. Experiments were conducted at an Mg:P molar ratio of 1.6, agitation of 300 rpm, and T = 20 °C.

To minimize NaOH consumption and reduce operational costs, a final pH of 9.0 was selected for the crystallization process. This pH value is widely reported in the literature for struvite crystallization and is frequently associated with high phosphorus recovery rates [26–28]. During the experiments, nucleation was observed after adding 25.0% of the total moles of NaOH required to reach the target pH (9.0) for WW1, 42.9% for WW2, and 33.3% for WW3. Based on these observations, a NaOH dosing strategy was defined for the continuous process to improve control over nucleation and crystal growth. To initiate nucleation, 30% of the total alkali required to reach the pH 9.0 was injected at the first injection point in the planar-OFC, while the remaining 70% was added at the second injection point (Fig. 1, n° 9).

3.2.2. *Determination of equilibrium concentrations*

After determining the NaOH dosage, subsequent experiments were conducted to investigate crystallization kinetics. Therefore, to transition from batch to continuous mode, it was essential to determine the equilibrium phosphate concentrations, the struvite solubility at various temperatures, and the induction time for crystallization.

According to Eq. (2), struvite's precipitation is followed by a decrease in the concentration of magnesium, ammonium, and phosphate ions with time until the heterogeneous equilibrium solid-liquid is established. At this point, the solution becomes saturated, the driving force for the crystallization process is null, and no precipitation occurs [29,30]. The molar decrease in Mg^{2+}, NH_4^+, and PO_4^{3-} concentrations ($C_{initial} - C_{steady\text{-}state}$) in equal proportion is indicative of struvite precipitation. Thermodynamic aspects of struvite precipitation and solubility were discussed in Section S5 (Supplementary material). For all experiments, the Mg:N:P molar ratio was assumed to be 1:1:1 since calcium phosphate precipitation was not detected. The difference between the initial and steady-state concentrations of Ca^{2+} remained practically unchanged (Tables 1 and 3), indicating that Ca^{2+} did not participate in the precipitation reaction. This outcome was expected, given that magnesium phosphates precipitate faster than Ca-phosphates and typically dominate under the operational conditions applied in this study [28].

At a final pH = 9.0, it was found that the equilibrium for struvite formation was achieved after 20 min of reaction (Fig. 3a). As the initial concentration of magnesium increased (from Mg:P of 1.0 up to 1.6), the equilibrium concentration of phosphate decreased (Fig. 3b).

The minimum struvite solubility product (K_{sp}) ranges from $10^{-9.41}$ to $10^{-13.36}$, with the most commonly used value in engineering being $10^{-12.6}$, which has been applied in this work to determine saturation indexes (SI) for each tested condition [30–35]. The results indicated that higher initial Mg:P molar ratios enhanced the extent of the reaction, shifting the chemical equilibrium of Eq. (2) toward struvite formation. It is well established that a higher initial SI promotes both the nucleation and crystal growth rates of struvite [25,36,37]. At the final pH studied, however, the nucleation and growth rates were almost negligible for Mg:P molar ratios of 1.5 and 1.6 since SI < 0 (see Table S2). This indicates that, at these molar ratios, further increasing the initial magnesium concentration does not provide an effective means of enhancing precipitation rate. Instead, supersaturation must be increased by adjusting other operating parameters, such as final pH, temperature, or phosphate concentration in the medium.

As shown in Section S5 (Supplementary material), for Mg:P molar

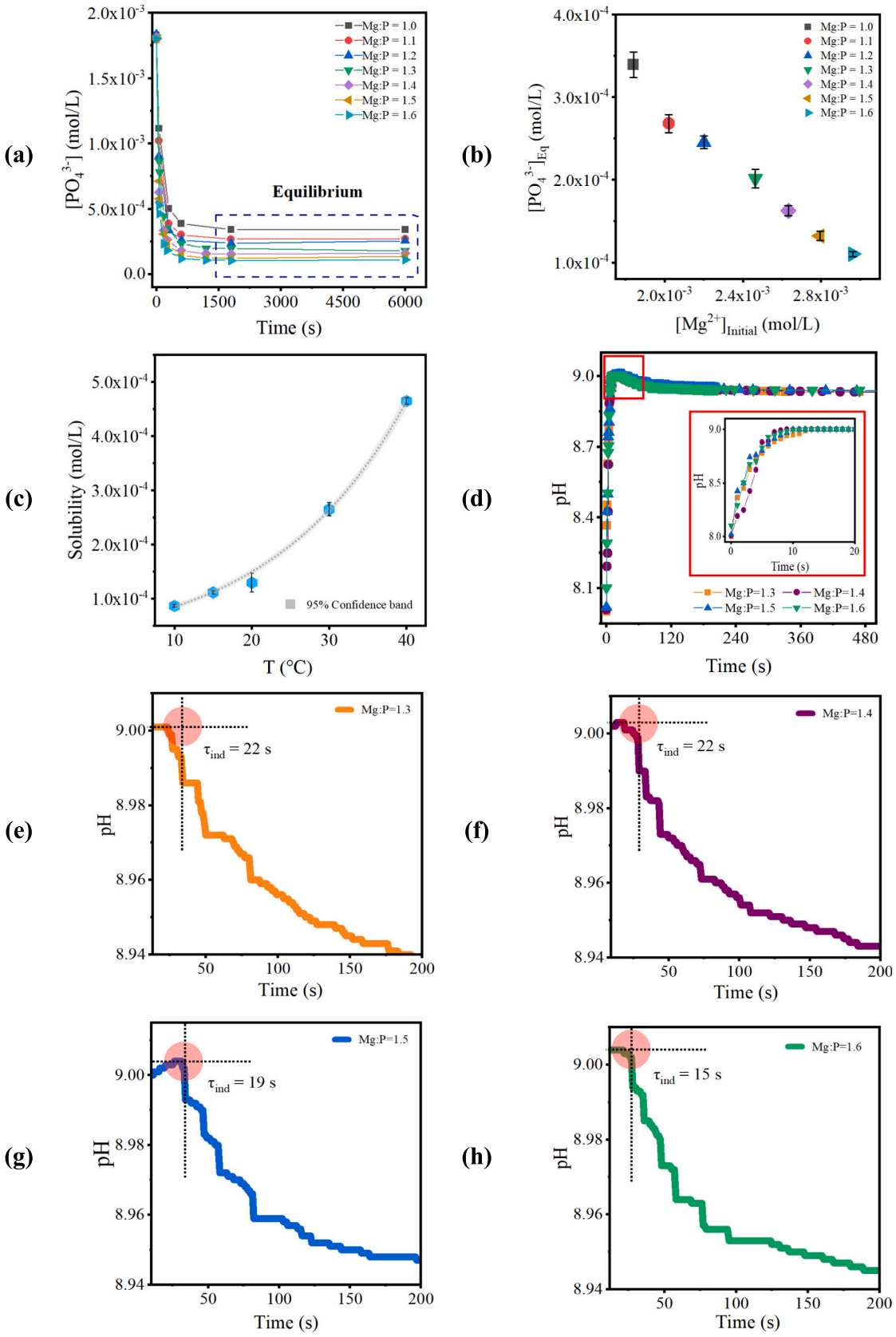


Fig. 3. Batch crystallization using WW1, different initial Mg:P molar ratios, final pH = 9, T = 20 °C, agitation of 300 rpm. (a) Phosphate concentration over time; (b) equilibrium phosphate concentrations; (c) solubility curve of struvite as function of temperature; (d) pH variation over time; (e-h) determination of induction time for struvite crystallization using the tangent method.

ratios between 1.0 and 1.4, the solution remains supersaturated; under these conditions, additional precipitation can be achieved either by further increasing the final pH to enhance supersaturation or by seeding the solution with small struvite crystals [38,39]. The best condition (Mg:$P = 1.6$ and final pH = 9.0) yielded a maximum phosphorus recovery of 93.9 ± 0.2%. However, it is important to note that these conclusions are based on batch experiments. In contrast, under continuous operation, kinetic constraints became more relevant. In this case, lower initial Mg:P ratios (i.e., 1.0–1.2), although thermodynamically favorable, resulted in lower R_P recoveries, likely due to insufficient nucleation and crystal growth rates under the imposed residence times. Thus, these conditions were not thoroughly evaluated. Therefore, despite the limited thermodynamic benefit observed in batch conditions at Mg:P molar ratios above 1.5, higher magnesium dosages were required in continuous operation to achieve adequate supersaturation and sustain crystallization kinetics.

3.2.3. Solubility versus temperature

The most promising final pH and initial magnesium concentration (Mg:$P = 1.6$) were established based on the experimental results presented in the previous sections. Under these conditions, the solubility (S) of struvite was experimentally determined across a temperature range of 10 to 40 °C, as represented in Fig. 3c. Understanding the variation of struvite's solubility over temperature is critical because this parameter directly influences the crystallization process. This knowledge is essential for designing and implementing crystallization processes that account for environmental factors, such as climate variability (e.g., fluctuations in ambient temperature), as well as operational constraints within WWTPs. As temperature increases, struvite's solubility also rises, which can reduce the yield of phosphorus recovery. Several studies have explored how struvite solubility changes with temperature. The solubility data obtained in the present work are consistent with the trends observed in other studies [20,31,40–43], supporting the reliability of the results.

The experimental data followed an exponential fit (Eq. (3)), where S is in mol L^{-1} and T* is in °C. The narrow confidence intervals suggest that the model is suitable for describing the experimental data.

$$S = (4.8 \pm 0.1) \times 10^{-5} \times e^{\left[(565 \pm 7) \times 10^{-4} \times T^*\right]} \quad (3)$$

3.2.4. Determination of the induction time

The induction time (τ_{ind}) is defined as the time interval between reaching a given supersaturation and the appearance of a stable solid phase (nucleation) [25]. According to Eq. (2), struvite formation releases protons, resulting in a slight decrease in pH [21], as shown in Fig. 3d. Thus, τ_{ind} was determined as the time elapsed between pH adjustment to 9.0 and the first detectable pH decrease. It should be noted that this definition represents an operationally defined induction time, based on a measurable macroscopic signal, rather than the exact microscopic onset of nucleation, which may occur earlier but is not directly observable by this method. Previous studies identified τ_{ind} using pH drops of 0.005 and 0.05 units [32,33,37,44]. In this study, a decrease of 0.01 units was used, which falls within the reported range.

After NaOH addition, the pH rapidly increased to 9.0 within approximately 10 s and stabilized briefly before decreasing due to nucleation (Fig. 3d). This behavior was consistent for all initial Mg:P molar ratios (1.3–1.6), reflecting uniform initial behavior of the system. The corresponding τ_{ind} were then determined for each Mg:P ratio (Fig. 3e–h). Increasing the initial magnesium concentration decreased τ_{ind}. These results indicate that higher supersaturation levels generally yield lower τ_{ind} values, thereby accelerating the onset of crystallization [25,29]. Although the variations in τ_{ind} across the tested Mg:P molar ratios were not drastic, the trend suggests that even minor changes in magnesium dosage can influence the nucleation kinetics. These findings underscore the importance of accurately controlling the initial magnesium concentration to improve process efficiency. Consequently, for continuous operation, the residence time in the planar-OFC reactor must exceed 22 s, as this value corresponds only to the period required for nucleation. Since the time required for crystal growth is unknown, a longer residence time is essential to ensure both nucleation and sufficient crystal growth, thereby promoting effective nutrient recovery as struvite.

3.3. Continuous crystallization in the planar-OFC

Sample "WW1" was used to study continuous struvite crystallization in the planar-OFC by investigating pH conditions, assessing the influence of the Mg:P molar ratio on the precipitation kinetics, and evaluating the effects of net flow rate and temperature on struvite formation.

3.3.1. Effect of the final pH

The impact of the final pH on the crystallization process was assessed at a sample flow rate (Q_W) of 16 mL/min, corresponding to a residence time of approximately 4 min within the reactor. This time encompassed the nucleation process (< 22 s) and provided additional time (~3.5 min) for crystals to grow and/or aggregate.

To achieve phosphorus recoveries (R_P) exceeding 80% (Fig. 4), the initial Mg:P molar ratio must be 1.6, regardless of whether the final pH was 9.0 or 9.5. For this ratio, at a final pH of 9.0, R_P was 80.4% ± 0.6%, whereas at 9.5, it increased slightly to 85.2% ± 0.8%. When evaluated on a normalized basis (kg of reagent consumed per kg of P recovered; Table S3), operating at higher pH values results in a substantial increase in NaOH consumption, with only a marginal improvement in phosphorus recovery. For example, at Mg:$P = 1.6$, NaOH consumption increases from 6.8 to 12.0 kg/kg of P recovered when increasing the final pH from 9.0 to 9.5, whereas $MgCl_2$ consumption decreases only slightly (from 5.8 to 5.1 kg/kg of P recovered). Similarly, operating at Mg:$P = 1.5$ and final pH = 9.5 yields an R_P (78.3% ± 0.8%) comparable to that obtained at Mg:P = 1.6 and final pH = 9.0 (80.4% ± 0.6%), but at the expense of significantly higher NaOH consumption (13.0 vs 6.8 kg/kg of P recovered).

Therefore, choosing a final pH of 9.0 and a Mg:P ratio of 1.6 offers a more cost-effective and resource-efficient approach to struvite crystallization, reducing unnecessary chemical use while ensuring high phosphorus recovery.

3.3.2. Kinetics of precipitation

Multiple studies have reported that the formation rate of struvite can be modeled using a first-order kinetic model (Table S4) by integrating Eq. (S8) (Section S6 – Supplementary material), resulting in Eq. (4).

$$\left[PO_4^{3-}\right]_t - \left[PO_4^{3-}\right]_{eq} = \left(\left[PO_4^{3-}\right]_0 - \left[PO_4^{3-}\right]_{eq}\right) \times e^{-k_{ap}t} \quad (4)$$

Eq. (4) is a modified expression of the first-order kinetic model, where [] represents the molar concentration of phosphate ions, the

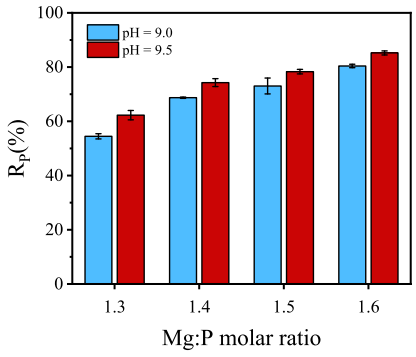


Fig. 4. Effect of pH on phosphorus recovery during continuous struvite crystallization using the WW1 sample. Q_w = 16 mL/min, T = 20 °C, f = 4 Hz, x_0 = 5.8 mm.

subscripts *t*, *0,* and *eq* denote time *t*, time 0, and equilibrium, respectively [45]. The equilibrium phosphate concentrations were independently measured via batch mode crystallization experiments, as outlined in Section 3.2.2. These experimentally derived values define the limit of phosphate removal from the aqueous medium and were not treated as adjustable fitting parameters. Plots of the experimental trials performed at different initial Mg:P molar ratios, with a final pH of 9.0 during crystallization, are presented in Fig. 5a.

The curves display an exponential decay trend where the proposed pseudo-first-order kinetic model provides an excellent fit to the experimental variation of $[PO_4^{3-}]_t - [PO_4^{3-}]_{eq}$ within the investigated operating window. It should be noted, however, that this model represents a macroscopic description of the overall process, which encompasses multiple phenomena (e.g., nucleation, crystal growth, effects of supersaturation, and hydrodynamics) but does not explicitly account for their individual contributions. As such, the model provides a reliable and practical description within the range of operating conditions investigated. However, its predictive capability under significantly different conditions cannot be guaranteed, as changes in system dynamics may alter the dominant controlling mechanisms. Table S5 shows the values of k_{ap} (expressed in both s^{-1} and h^{-1}) determined by model fitting, along with the corresponding coefficients of determination (R^2). The strong agreement between experimental data and model predictions is supported not only by the high value of R^2 (0.99), but also by the low values of the sum of squared residuals (SSR) obtained, which were 5.8×10^{-9} (mol L^{-1})^2 for Mg:*P* = 1.3, 1.2×10^{-8} (mol L^{-1})^2 for Mg:*P* = 1.4, 1.4×10^{-8} (mol L^{-1})^2 for Mg:*P* = 1.5 and 1.9×10^{-9} (mol L^{-1})^2 for Mg:*P* = 1.6.

Additionally, the data in Fig. 5a demonstrate that, under the evaluated conditions, increasing both the initial Mg:P molar ratio and the residence time in the reactor improves phosphorus recovery during continuous struvite production. As shown in Fig. 5a, higher residence times consistently led to improved results across all tested Mg:P molar ratios. This trend can be attributed to the fact that the mean value of τ_{ind} was around 20 s, so longer residence times provide more opportunity for crystals to nucleate and grow. Moreover, the phosphate concentration under these conditions remained above the equilibrium level (Table S6), indicating that the system had not yet reached its maximum

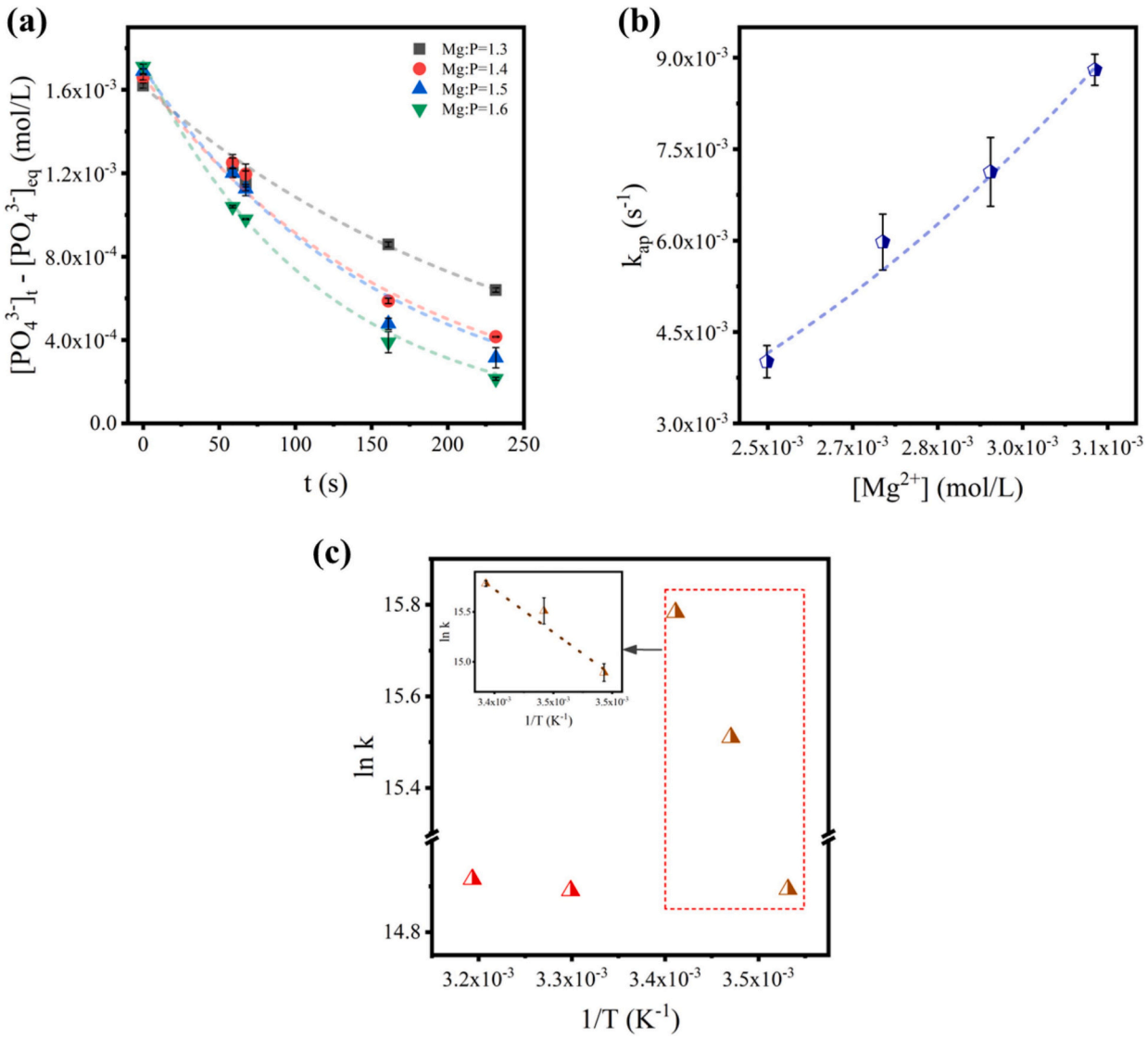


Fig. 5. (a) Comparison between experimental data and the exponential fitting (dashed line) obtained during continuous struvite crystallization in the planar-OFC at final pH = 9.0, T = 20 °C, f = 4 Hz, and x_0 = 5.8 mm. Each data point represents a different SD net flow rate (63 mL/min – 58.8 s; 55 mL/min – 67.4 s; 23 mL/min – 161.1 s; 16 mL/min – 231.5 s); (b) effect of the initial magnesium concentration on the apparent rate constant (k_{ap}) of struvite precipitation; (c) Arrhenius plot (ln k vs. T^{-1}) for isothermal continuous struvite crystallization in the planar-OFC at f = 4 Hz and x_0 = 5.8 mm, final pH = 9.0, and initial Mg:P = 1.6. The red triangles represent outliers.

crystallization potential and that further increases in residence time would likely enhance phosphorus recovery. However, from a process perspective, increasing residence time necessarily reduces the reactor's treatment capacity, highlighting a trade-off between recovery efficiency and productivity. One practical strategy to overcome this limitation without compromising throughput is to assemble multiple planar-OFC reactors in series. This configuration enables higher overall recovery by effectively increasing the cumulative residence time, while maintaining the net flow rate of SD and improving process scalability. It is important to note that the best condition identified for the crystallization process using the planar-OFC ($Q_W = 16$ mL/min and Mg:$P = 1.6$), which yielded an R_P of 80.4% ± 0.4%, represents the optimal performance within the experimental range investigated in this study, rather than a global process optimum. These results are consistent with those reported by studies that produce struvite by batch and continuous processes (Tables S1 and S4).

The comparison between the results of this study and those reported in the literature (Table S4) shows that the apparent rate constants fall within the reported range on an order-of-magnitude basis. However, direct comparison of apparent kinetic constants across different studies must be approached with caution, as these values are strongly dependent on operating conditions, including supersaturation levels, influent composition, initial Mg:P molar ratio, reactor configuration, and hydrodynamic regime [46,47]. Within this context, the apparent rate constants obtained in the present study fall within the upper range of values reported in the literature. Although direct comparisons of apparent rate constants across studies are limited by differences in operating conditions, the planar-OFC reactor achieves comparable kinetic performance at significantly lower residence times (4.3 min) and with a small reactor volume (69 mL), highlighting its potential for process intensification. In contrast, most literature reports comparable kinetics under batch operation or under substantially longer residence times. This indicates that the planar-OFC configuration provides favorable hydrodynamic and mass transfer conditions that support efficient crystallization within reduced processing times. The performance advantages of the planar-OFC reactor for struvite production are presented in Section S7 of the Supplementary material. Nevertheless, a rigorous assessment of reactor performance relative to conventional systems (e.g., CSTR or fluidized bed reactors) would require a direct comparison under identical, controlled conditions, which is beyond the scope of the present study.

As shown in Section S6, under the experimental conditions investigated, NH_4^+ remained in excess and did not act as a rate-limiting species. This behavior was also evident in the mass balance results (Fig. S5), where the NH_4^+ concentration showed small variations over time ($C_t/C_0 \approx 1$), in contrast to the pronounced depletion of phosphate and magnesium during struvite formation. Accordingly, the contribution of ammonium to the precipitation rate was neglected, and w was assumed to be zero. Additional support for this assumption is provided by the comparison between WW1 and WW2 (Section 3.4). Despite a twofold difference in initial NH_4^+ concentration, both systems exhibited nearly identical phosphate recovery under the same operational conditions and reaction time (4.3 min). This behavior indicates that within the investigated range (239–492 mg/L), ammonium concentration did not exert a controlling influence on the precipitation kinetics. While this justifies assuming $w = 0$ for the conditions studied, caution should be taken when extending this assumption beyond the evaluated concentration range.

As expected, the k_{ap} values are directly dependent on the initial magnesium concentration (Table S5). This trend, also reported in previous studies, reinforces the critical role of magnesium ions in influencing the kinetics of struvite precipitation [21,48–50]. Therefore, it is theoretically expected that the relationship between k_{ap} and Mg^{2+} concentration follows the power-law form: $k_{ap} = k \times [Mg^{2+}]^n$. Here, k represents a unified kinetic constant under the studied conditions, which can be determined from the experimental data obtained. While k is independent of reactant concentrations within this framework, it may still reflect the specific chemical environment (e.g., temperature and solution composition) [51].

The power-law model fitted well the experimental data ($k = (7 \pm 1) \times 10^6$; $n = 3.6 \pm 0.4$; $R^2 = 0.984$), confirming that the rate of crystallization is strongly dependent on the availability of magnesium in the system (Fig. 5b). A reaction order greater than 1 implies that small increases in Mg^{2+} concentration result in large enhancements in the reaction rate. The combination of the power-law model and Eq. (4) into a single expression (Eq. (5)) characterizes the system's behavior and also predicts the temporal evolution of phosphate consumption during the crystallization reaction.

$$\left[PO_4^{3-}\right]_t - \left[PO_4^{3-}\right]_{eq} = \left[(1.73 \pm 0.02) \times 10^{-3}\right] \times e^{-(7\pm1)\times10^6 \times \left[Mg^{2+}\right]_0^{(3.6\pm0.4)} \times t} \quad (5)$$

In addition to crystallization performance, preliminary insights into crystal size distribution (CSD) were obtained by comparing solids from batch and continuous (planar-OFC) crystallization under similar conditions (final pH = 9.0, initial Mg:P molar ratio of 1.5, T = 20 °C). In batch mode, solids were collected after equilibrium was reached (20 min); in continuous operation, they were collected at the reactor outlet after a residence time of 4.3 min. The results (Fig. S6) show that both systems exhibit a bimodal CSD, indicating simultaneous nucleation and crystal growth [52]. Notably, the continuous process achieved a similar CSD pattern in a significantly shorter time, highlighting its potential for process intensification. This suggests that transitioning to continuous operation with the planar-OFC does not fundamentally alter the crystallization pathway under the tested conditions. However, the predominance of fine particles may pose challenges for downstream solid–liquid separation, particularly filtration. These observations highlight the need to improve crystal size and promote aggregation to enhance process integration and product handling. Accordingly, ongoing work is focused on optimizing operating conditions and hydrodynamics to promote crystal growth, increase mean particle size, and narrow the CSD, thereby facilitating more efficient separation and recovery of the solid product.

3.3.3. Estimation of the activation energy

The activation energy (E_a) is the minimum amount of energy needed to start a reaction. In general, a lower activation energy leads to a quicker reaction rate [53]. The value of E_a can be calculated according to the linearization of the Arrhenius-type equation [29]:

$$\ln k = \ln A - \frac{E_a}{RT} \quad (6)$$

where k is the kinetic rate constant, A is a constant called the frequency factor, E_a is the activation energy, T is the absolute temperature, and R is the gas constant (8.314 J/K/mol) [43]. Five isothermal experiments were performed using the planar-OFC operating at $f = 4$ Hz and $x_0 = 5.8$ mm to evaluate the influence of temperature on the apparent rate performed at a final pH of 9.0, and an initial Mg:P molar ratio was 1.6, with net flow rates (Q_W) of 16, 23, 55, and 63 mL/min. For each temperature, k_{ap} values were determined by Eq. (4).

A linear relationship between $\ln k$ and T^{-1} was observed for the data obtained at 10, 15, and 20 °C (Fig. 5c), supporting the applicability of the Arrhenius model within this temperature range. However, two points (red triangular points), obtained at 30 °C and 40 °C, deviate significantly from the others. Rather than representing random experimental outliers, this deviation likely reflects a shift in the crystallization regime at higher temperatures. Such behavior may be associated with changes in struvite solubility, initial supersaturation, and the number of crystals present at the onset of the process, all of which influence the crystallization driving force and the relative contributions of nucleation and growth mechanisms. Further details are provided in Section S8.

Accordingly, the activation energy was estimated as 59 ± 7 kJ/mol. This value should be interpreted as an apparent activation energy valid

within the 10–20 °C range where linear behavior was observed, rather than as a general kinetic parameter for struvite crystallization over the entire temperature range investigated. The activation energy for struvite's crystallization is typically estimated under batch-mode conditions using synthetic solutions, commonly based on data from three temperature points. Under these experimental conditions, values reported in the literature ranged from 25.6 to 64.5 kJ/mol (Table S7) and were influenced by factors such as supersaturation, ionic composition, pH, temperature, and operational mode. The E_a estimated in the present study (59 ± 7 kJ/mol) falls within this range and shows good agreement with published data. Unlike the studies, summarized in Table S7, which were based on batch-mode crystallization using synthetic solutions, this work employed continuous struvite crystallization from SD samples collected from a municipal WWTP – a more complex aqueous medium. This highlights that comparable activation energies can still be estimated under more complex and realistic conditions.

Additionally, temperature has a significant impact on the continuous crystallization process. When T ≥ 30 °C, crystallization was hindered because struvite solubility increased. Conversely, temperatures <20 °C did not improve phosphorus recovery, as the kinetic rate constant decreases at lower temperatures, slowing struvite formation and extending the time required to reach equilibrium. The lowest phosphate concentrations achieved with the planar-OFC were 0.87 mM at 10 °C, 0.52 mM at 15 °C, and 0.32 mM at 20 °C, confirming that 20 °C is the optimal operating temperature for this process. In a pilot-scale prototype, ambient temperature fluctuations can be managed to optimize phosphorus recovery. On hotter days, struvite formation may decrease. One practical strategy to help maintain process efficiency could be to increase the supersaturation (e.g., by raising the pH). However, this should be regarded as a tentative consideration, since the extent to which supersaturation can offset temperature effects was not systematically evaluated in this study. Alternatively, on colder days, the planar-OFC can be operated at lower temperatures, where extending the reactor residence time is essential to sustain high recovery rates.

The mass balance for all conditions evaluated under planar-OFC continuous operation is presented in Tables S8–S11 (Section S9).

3.4. Performance of the continuous crystallization process

Based on the findings discussed in the previous sections, the best operational conditions for the continuous crystallization process within the design space were identified as follows: a final pH of 9.0, an initial Mg:P molar ratio of 1.6, a temperature of 20 °C, and a sidestream net flow rate of 16 mL/min. These conditions were applied to crystallize struvite from three SD samples to validate the process's performance and the proposed kinetic model. Table 3 presents the experimental data obtained after crystallization. A comparison of the data presented in Tables 1 and 3 reveals a substantial reduction in phosphate concentration across all samples. In all cases, the recoveries of phosphate (R_P) exceeded 80%, confirming the effectiveness of the crystallization process and supporting the viability of the proposed continuous crystallization operation using the planar-OFC.

Table 3
Resume of the main parameters determined after the continuous crystallization using the planar-OFC applied to sidestream digestate samples WW1, WW2, and WW3.

Parameter	WW1	WW2	WW3
Phosphate (mg/L)	30.8 (±0.6)	29 (±3)	22 (±1)
Ammonium (mg/L)	454.0 (±0.4)	213.5 (±0.6)	597 (±6)
Magnesium (mg/L)	39.57 (±0.2)	32 (±2)	78.8 (±0.7)
Calcium (mg/L)	40.9 (±0.5)	10.4 (±0.2)	30.3 (±0.9)
Sodium (mg/L)	378.6 (±0.8)	224.7 (±0.2)	408 (±5)
Potassium (mg/L)	111 (±1)	80.7 (±0.6)	175 (±1)
R_P (%)	80.4 (±0.4)	83 (±2)	95.0 (±0.4)
Mg:N:P ratio[a]	1:1:1	1:1:1	1:1:1
[PO_4^{3-}] predicted[b]	31.3	46.0	39.5

[a] Based on the reduction in molar concentrations of Mg, N, and P.
[b] Predicted by the kinetic model proposed.

The yield of struvite production reached 0.4 kg/m^3 of SD for WW1 and WW2, and 1.1 kg/m^3 of SD for WW3. The final concentration of NH_4^+ ions decreased slightly and remained relatively high across all samples. This outcome was expected, as ammonium ions account for only about 7% of the total struvite mass [23]. Consequently, nitrogen recoveries were relatively low (average 10 ± 2%), indicating that, under the studied conditions, struvite production primarily served as a phosphorus recovery pathway, with limited nitrogen capture. Nevertheless, ongoing pilot-scale studies by our group are exploring strategies to enhance nitrogen recovery, including the dosing of phosphate from alternative and low-cost sources. This approach aims to rebalance the Mg:N:P stoichiometry and promote additional struvite formation, thereby increasing the overall nitrogen recovery potential of the process.

Regarding magnesium, this ion was intentionally dosed in excess to enhance P-recovery, resulting in relatively high residual magnesium concentrations. The corresponding magnesium recoveries (R_{Mg}) averaged 51 ± 7%. Despite these results, reductions in the molar concentrations of Mg^{2+}, NH_4^+, and PO_4^{3-} across all samples occurred in approximately equimolar proportions (Tables 3 and S11). The equimolar reduction strongly suggests that struvite was the predominant precipitated solid during crystallization. The crystal morphology (Figs. S7 and S8) further supports this conclusion. Additional analysis of the recovered solid is presented in Section 3.5.

Concerning other ions, the final calcium concentration remained relatively unchanged in the WW1 and WW2 samples, but decreased by nearly 43% in WW3. This suggested that calcium may have precipitated in some form, possibly as calcium phosphate or calcite [54]. When calcium is present in water, the precipitated solid tends to become more irregular, with surfaces covered by fine particles, and crystals may exhibit cracks or structural imperfections [55,56]. These features were visible (Fig. S8e and f) and corresponded to the crystals obtained from WW3. However, compositional analysis of the solids revealed a low calcium content (<1 wt%), and XRD Rietveld refinement confirmed that struvite was the dominant crystalline phase. These results may suggest that calcium was not significantly incorporated into the crystalline structure. Therefore, the observed decrease in aqueous calcium concentration is most likely associated with adsorption onto the surfaces of the formed crystals, followed by removal during the washing step with deionized water, thereby improving the purity of the solid. Nevertheless, the formation of other crystalline or amorphous calcium-containing phases cannot be entirely excluded, particularly given the complexity of the digestate matrix. Previous studies have shown that struvite purity exceeds 98% when the Mg:Ca molar ratio exceeds 4 [38]. In WW3, the initial Mg:Ca molar ratio (after Mg dosing) was 5.8, which may explain the observed Mg:N:P molar ratio of 1:1:1 and high purity obtained.

The final sodium concentration increased due to the addition of NaOH. However, no precipitation of sodium ions was observed. In contrast, potassium concentrations decreased by 2.6% to 9.3%, suggesting the possible formation of struvite-(K), $MgKPO_4$ [34,55].

Finally, the kinetic model presented in Eq. (5) was applied to predict the final phosphate concentration for each SD sample. For WW1 and WW2, the model predictions closely matched the experimental data. However, for WW3, the measured phosphate concentration was 44.3% lower than the predicted value. In general, struvite precipitation involves nucleation, crystal growth, and aggregation, which collectively determine the overall crystallization rate [25]. The kinetic model developed in this work is a macroscopic, liquid-phase species-depletion model, calibrated under relatively low phosphate concentrations (<200 mg/L). Within this range, the model adequately described phosphate consumption over time (as observed for WW1 and WW2 samples). However, the consumption of phosphate couldn't be fully represented by a single species-depletion expression when operating across significantly different supersaturations. This was observed in the WW3 sample (initial

phosphate concentration of 445 mg/L), once the system suddenly shifted to a substantially higher supersaturation. Under these conditions, changes in supersaturation may have altered the relative contributions of nucleation and crystal growth rates, and may also have promoted secondary phenomena such as rapid nucleation bursts, particle-particle interactions, and aggregation, resulting in greater phosphate ion consumption and higher struvite yield [36,37]. These mechanisms were not explicitly accounted for in the proposed kinetic model.

Also, the model estimated the half-life time ($t_{1/2}$) of the crystallization process to be 79 s. Since the residence time in the reactor was approximately three times longer than $t_{1/2}$, it provided sufficient time for the reaction to proceed, enabling good phosphate recovery.

The results presented herein are based on short-term operation (≤30 min) under controlled conditions, where no fouling or significant crystal accumulation was observed. While these findings support the robustness of the proposed kinetic model within the tested timeframe, long-term operational aspects such as solid buildup, hydrodynamic changes, and maintenance requirements require further investigation and are currently being addressed in ongoing pilot-scale studies conducted by our investigation group.

The economic feasibility of struvite production is inherently linked to reagent consumption, operational costs, and potential revenues from product valorization [57]. In this context, normalizing reagent demand per unit of phosphorus recovered provides a more robust basis for comparison across different systems. Based on this approach, the recovery of 1 kg of phosphorus (equivalent to 7.9 kg of struvite) from the studied SD samples required 5.8 kg of $MgCl_2$ and 6.8 kg of NaOH for WW1, 4.5 kg of $MgCl_2$ and 5.6 kg of NaOH for WW2, and 5.1 kg of $MgCl_2$ and 4.7 kg of NaOH for WW3. These results indicate that higher initial phosphate concentration and higher recovery efficiency reduce reagent consumption per unit of phosphate.

Although numerous struvite recovery technologies have been reported, direct economic comparisons are limited by differences in operational conditions and system configurations [57]. Moreover, the planar-OFC operates at lab scale, with a maximum treatment capacity of 23 L/day and a daily production of 6–9 g of struvite. This limits meaningful comparison with full-scale technologies, such as Pearl (1600 kg/day) or AirPrex (1000 kg/day) [6,58], given the substantial disparity in production scale.

Finally, the economic return from struvite valorization is influenced by market conditions, as reported prices vary widely in the literature (approximately 245–1000 €/ton) [7], making it difficult to define a representative revenue value. These factors highlight the need for case-specific techno-economic assessments, which will be addressed in future pilot-scale studies.

3.5. Quality of the produced struvite

The crystals collected at the reactor's outlet were analyzed in the microscope, and the typical orthorhombic prismatic shape of struvite was visualized [56] (Fig. S7). The crystals exhibited a variety of morphologies commonly reported for struvite, including needle-like, rod-like, dendritic, and X-shaped structures [26,34,49,56,59,60]. The WW3 crystals exhibited a stronger tendency to agglomerate and appeared more elongated, with irregular, less-defined shapes. The SEM analysis (Fig. S8) was performed on dried, collected samples, in which mechanical stress associated with drying and scraping induced crystal fragmentation and increased surface roughness. The solids obtained from WW2 and WW3 exhibited rougher surfaces, with cracks and irregular edges. These features are attributed to sample handling and do not reflect the intrinsic quality of the crystals formed during crystallization.

The FTIR analysis of all solid samples exhibited similar spectra, consistent with the characteristic pattern of pure struvite (Fig. 6a). The XRD patterns (Fig. 6b–d) clearly indicate that the solids are primarily composed of orthorhombic struvite (Section S10), although minor amounts of other cations (e.g., Ca, Na, and K) were detected in the chemical analysis. The diffractograms display well-defined peaks that coincide with those of the standard reference pattern for struvite [61], with no extra peaks indicating impurities or secondary phases, such as dittmarite or magnesium phosphate. Several authors have observed similar trends in their investigations [33,37,43,44,62–66].

Struvite recovery comparisons were performed (Fig. 6e), where all samples exhibit the characteristic elemental profile of struvite,

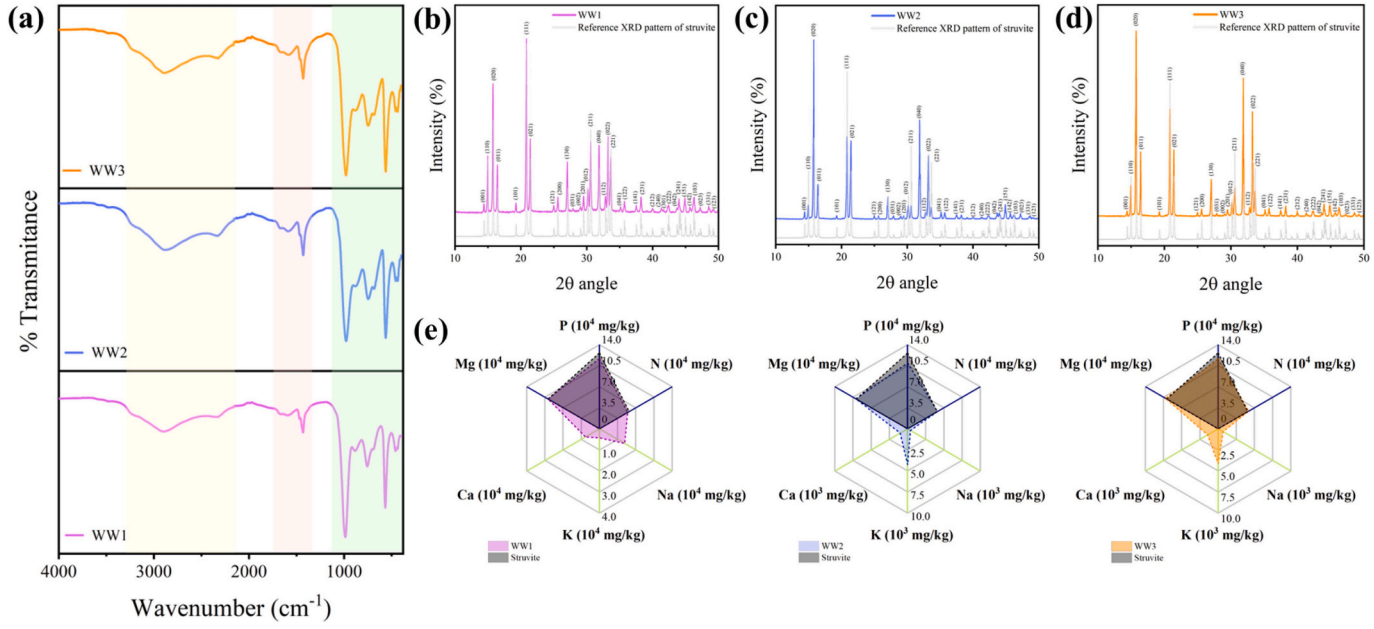


Fig. 6. (a) FTIR spectra of struvite samples: WW1 (purple), WW2 (blue), and WW3 (orange); XRD diffraction patterns of struvite samples from (b) WW1, (c) WW2, and (d) WW3; (e) chemical composition of struvite (WW1, WW2, and WW3) compared with the standard struvite composition (grey), expressed in terms of primary and secondary inorganic macronutrients. The blue axis indicates that Ca, K, and Na share the same scale, while the green axis indicates that P, Mg, and N share the same scale.

confirming the successful crystallization of the target compound. The chemical composition of the crystallized solids, expressed in mg of inorganic constituent per kg of solid, is illustrated in Fig. 6e. Each radar plot compares the nutrient composition of struvite recovered from wastewater (WW1, WW2, and WW3) with standard struvite (shown in light grey).

The results indicate that all samples exhibit the typical elemental profile of struvite, confirming successful crystallization of the target compound. However, small amounts of other cations (Ca, Na, and K) were also detected, suggesting possible co-precipitation with struvite. It has been reported that struvite crystals typically exhibit a strongly negative zeta potential over the pH range of 8.5–10.5. Under these conditions, higher absolute zeta potential values correspond to increased surface charge density, which can promote electrostatic interactions with positively charged ions present in solution (e.g., Na, Ca, and K), attracting them to the solid's surface [67]. Quantitative analysis of the solid after dissolution in 0.5% nitric acid solution revealed high purities of 95.8 ± 0.2% for WW1, 92.6 ± 0.1% for WW2, and 95.7 ± 0.1% for WW3.

Following Regulation 2019/1009, the produced struvite is classified as a solid inorganic macronutrient fertilizer, with mean contents of nitrogen, phosphorus (as P_2O_5), and magnesium (as MgO) of 5.7 ± 0.2%, 26.2 ± 0.6%, and 16.6 ± 0.1%, respectively (Table S13). Compliance with the EU Regulation on fertilizing materials was assessed with particular focus on regulated heavy metals [68]. Zinc was detected in solid 1 (from WW1) and solid 3 (from WW3) at concentrations of 1169 ± 13 mg/kg and 456 ± 13 mg/kg, respectively, both below the regulatory limit of 1500 mg/kg. The concentrations of Cu, Cd, Cr(VI), Hg, As, Ni, and Pb in struvite samples were below the Limit of Detection (LOD) of the ICP-OES analysis (LODs provided in Table S14), indicating full compliance with the established thresholds. Other elements not subjected to regulatory limits were detected at low concentrations, including strontium (8 ± 1 mg/kg), iron (45 ± 15 mg/kg), and manganese (1.1 ± 0.2 mg/kg) in WW1, and silver (212 ± 30 mg/kg) in WW3. These results confirm the high chemical quality of the recovered struvite, as evidenced by its regulated inorganic composition. However, it should be noted that microbiological parameters, including pathogen presence, were not evaluated in this study. Therefore, while the material meets chemical criteria defined by EU Regulation, further analyses would be required to assess its full agronomic and sanitary suitability for use as fertilizer.

4. Conclusions

The planar-OFC technology was successfully employed for the continuous crystallization of struvite from liquid sidestream digestate samples, demonstrating efficient phosphorus recovery under optimized conditions. The results indicate that phosphorus is preferentially recovered, whereas nitrogen recovery remains limited due to the intrinsic composition of struvite. The best conditions within the investigated experimental range were determined (pH = 9.0, initial Mg:P molar ratio of 1.6, temperature of 20 °C, and residence time ≈ 4 min), although the system had not yet reached its maximum crystallization potential, indicating that further improvements may be achieved under extended residence times or alternative reactor configurations. Despite the ionic composition, P recovery efficiencies above 80% were achieved at a final pH of 9, with a maximum struvite yield of 1.1 kg/m^3 of wastewater. Multivariate optimization using Design of Experiments will be addressed in future work to refine parameter interactions and improve process performance during pilot-scale implementation. Energy consumption will also be quantified using normalized metrics (e.g., kWh/kg P) to enable comparison with conventional systems. The rate of struvite production was well described by an apparent kinetic model, exhibiting a first-order dependence on PO_4^{3-} and a 3.56-order dependence on Mg^{2+} within the studied conditions, with rate constants >14 h^{-1} and an apparent activation energy of 59 ± 7 kJ/mol. Structural and compositional analyses confirmed that the recovered solids were predominantly orthorhombic struvite, the main crystalline phase, with overall chemical purities exceeding 92% in all samples. All struvite samples complied with EU Regulation 2019/1009 on fertilizing materials regarding macronutrient composition and regulated heavy metal content, demonstrating high chemical quality. However, as pathogen presence was not evaluated within the scope of this study, no conclusions can be drawn regarding microbiological safety. Therefore, additional analyses would be required to confirm the full agronomic and sanitary suitability of the recovered product for fertilizer applications. In conclusion, the planar-OFC represents a promising, potentially scalable alternative for enhancing nutrient recovery in municipal WWTPs and could address some of the limitations associated with traditional struvite production technologies. Moreover, ongoing work indicates that the use of alternative magnesium sources can substantially reduce reagent costs (by approximately 60–70%), further improving the economic feasibility of the process. Overall, these findings highlight the strong potential of the planar OFC for efficient, cost-effective phosphorus recovery.

CRediT authorship contribution statement

Luiza Sena: Writing – original draft, Visualization, Validation, Methodology, Investigation, Formal analysis. **Catarina Cruzeiro:** Writing – review & editing, Supervision, Investigation. **António Ferreira:** Writing – review & editing, Supervision, Investigation, Funding acquisition, Conceptualization. **Vítor J.P. Vilar:** Writing – review & editing, Supervision, Investigation, Funding acquisition, Conceptualization.

Declaration of competing interest

The authors declare the following financial interests/personal relationships which may be considered as potential competing interests: Given his role as a coordinating editor in Chemical Engineering Journal (CEJ), Vítor Vilar had no involvement in the peer review of this article and had no access to information regarding its peer review. Full responsibility for the editorial process for this article was delegated to another journal editor. If there are other authors, they declare that they have no known competing financial interests or personal relationships that could have appeared to influence the work reported in this paper.

Acknowledgements

This work was supported by: i) LiquidMining project, with reference COMPETE2030-FEDER-00861300, funded by the European Regional Development Fund (ERDF) through COMPETE2030 and by national funds through Fundação para a Ciência e a Tecnologia, I. P. (FCT); and ii) WAVES project, with reference NORTE2030-FEDER-02716600, funded through the NORTE2030 program, under the Support System for the Creation of Scientific and Technological Knowledge – Integrated R&D Projects (SACCCT – IC&DT), call NORTE2030-2024-84. Access to the TAIL-UC facility, funded under QREN-Mais Centro Project ICT/2009/02/012/1890, is gratefully acknowledged. This research was also supported by Fundação para a Ciência e a Tecnologia, I.P./MECI through national funds: LSRE-LCM, UID/50020/2025 (https://doi.org/10.54499/UID/50020/2025); LEPABE, UID/00511/2025 (https://doi.org/10.54499/UID/00511/2025) and UID/PRR/00511/2025 (https://doi.org/10.54499/UID/PRR/00511/2025), ALiCE, LA/P/0045/2020 (https://doi.org/10.54499/LA/P/0045/2020), CFisUC, UIDB/04564/2020 (https://doi.org/10.54499/UIDB/04564/2020) and UIDP/04564/2020 (https://doi.org/10.54499/UIDP/04564/2020). Luiza Sena acknowledges her PhD scholarship supported by FCT, 2022.11876.BD (https://doi.org/10.54499/2022.11876.BD). Catarina Cruzeiro acknowledges her Postdoctoral Junior Leader Fellowship from "la Caixa" Foundation (ID 100010434) with the code LCF/BQ/PI23/11970038 and FCT for its financial support (2023.07750.CEECIND).

Appendix A. Supplementary data

Supplementary data to this article can be found online at https://doi.org/10.1016/j.cej.2026.179515.

Data availability

Data will be made available on request.

References

[1] International Fertilizer Association, Fertilizer Consumption - Historical Trends by Country or Region in the World From 1963-2023. https://www.ifastat.org/databases/graph/1_1, 2026.

[2] M. Sena, M. Seib, D.R. Noguera, A. Hicks, Environmental impacts of phosphorus recovery through struvite precipitation in wastewater treatment, J. Clean. Prod. 280 (2021) 124222, https://doi.org/10.1016/j.jclepro.2020.124222.

[3] B. Li, S.J. Ng, J.-C. Han, M. Li, J. Zeng, D. Guo, Y. Zhou, Z. He, X. Wu, Y. Huang, Network evolution and risk assessment of the global phosphorus trade, Sci. Total Environ. 860 (2023) 160433, https://doi.org/10.1016/j.scitotenv.2022.160433.

[4] S. Vinardell, J.L. Cortina, C. Valderrama, Environmental and economic evaluation of implementing membrane technologies and struvite crystallisation to recover nutrients from anaerobic digestion supernatant, Bioresour. Technol. 384 (2023) 129326, https://doi.org/10.1016/j.biortech.2023.129326.

[5] B. Lew, S. Phalah, C. Sheindorf, M. Kummel, M. Rebhun, O. Lahav, Favorable operating conditions for obtaining high-value struvite product from sludge dewatering filtrate, Environ. Eng. Sci. 27 (2010) 733–741, https://doi.org/10.1089/ees.2009.0279.

[6] E. Desmidt, K. Ghyselbrecht, Y. Zhang, L. Pinoy, B. Van Der Bruggen, W. Verstraete, K. Rabaey, B. Meesschaert, Global phosphorus scarcity and full-scale P-recovery techniques: a review, Crit. Rev. Environ. Sci. Technol. 45 (2015) 336–384, https://doi.org/10.1080/10643389.2013.866531.

[7] M. Muys, R. Phukan, G. Brader, A. Samad, M. Moretti, B. Haiden, S. Pluchon, K. Roest, S.E. Vlaeminck, M. Spiller, A systematic comparison of commercially produced struvite: quantities, qualities and soil-maize phosphorus availability, Sci. Total Environ. 756 (2021) 143726, https://doi.org/10.1016/j.scitotenv.2020.143726.

[8] S. Daneshgar, A. Callegari, A.G. Capodaglio, D. Vaccari, The potential phosphorus crisis: resource conservation and possible escape technologies: a review, Resources 7 (2018) 37, https://doi.org/10.3390/resources7020037.

[9] N. Cherkasov, S.J. Adams, E.G.A. Bainbridge, J.A.M. Thornton, Continuous stirred tank reactors in fine chemical synthesis for efficient mixing, solids-handling, and rapid scale-up, React. Chem. Eng. 8 (2023) 266–277, https://doi.org/10.1039/D2RE00232A.

[10] P. Cruz, C. Silva, F. Rocha, A. Ferreira, The axial dispersion of liquid solutions and solid suspensions in planar oscillatory flow crystallizers, AIChE J. 65 (2019), https://doi.org/10.1002/aic.16683.

[11] A.M.A. Ferreira, F.A.N. da Rocha, J.A.C. Teixeira, F.J.F.C. Freitas, MODULAR OSCILLATORY FLOW PLATE REACTOR, EP3439773B1, 2022. https://worldwide.espacenet.com/patent/search/family/058737693/publication/EP3439773B1?q=EP3439773B1.

[12] Patrícia da Conceição Ferreira Dias Cruz, Control of the Continuous Crystallization of Active Pharmaceutical Ingredients (APIs) in an Oscillatory Flow Crystallizer, in: PhD Thesis, Faculdade de Engenharia da Universidade do Porto, 2021. https://hdl.handle.net/10216/139201.

[13] T. McGlone, N.E.B. Briggs, C.A. Clark, C.J. Brown, J. Sefcik, A.J. Florence, Oscillatory flow reactors (OFRs) for continuous manufacturing and crystallization, Org. Process Res. Dev. 19 (2015) 1186–1202, https://doi.org/10.1021/acs.oprd.5b00225.

[14] D. Ferreira-Faria, F. Domingos-Moreira, M.R. Aires-Barros, A. Ferreira, A. M. Azevedo, Continuous precipitation of antibodies using oscillatory flow reactor: a proof of concept, Sep. Purif. Technol. 317 (2023) 123924, https://doi.org/10.1016/j.seppur.2023.123924.

[15] J. Ferreira, S. Araújo, A. Ferreira, J. Teixeira, J.M. De Campos, F. Rocha, F. Castro, Insulin nucleation kinetics in an oscillatory flow-based platform: protein crystallization as a highly reproducible separation process, Chem. Eng. Res. Des. 203 (2024) 453–466, https://doi.org/10.1016/j.cherd.2024.01.057.

[16] P. Cruz, F. Rocha, A. Ferreira, Crystallization of paracetamol from aqueous solutions in a planar oscillatory flow crystallizer: effect of the oscillation conditions on the nucleation kinetics, CrystEngComm 23 (2021) 6930–6941, https://doi.org/10.1039/D1CE00922B.

[17] P. Cruz, F. Rocha, A. Ferreira, Determination of the critical mixing intensity for secondary nucleation of paracetamol in an oscillatory flow crystallizer, CrystEngComm 20 (2018) 829–836, https://doi.org/10.1039/C7CE01940H.

[18] N.E.B. Briggs, U. Schacht, V. Raval, T. McGlone, J. Sefcik, A.J. Florence, Seeded crystallization of β- L -glutamic acid in a continuous oscillatory baffled crystallizer, Org. Process Res. Dev. 19 (2015) 1903–1911, https://doi.org/10.1021/acs.oprd.5b00206.

[19] L.R. Agnew, T. McGlone, H.P. Wheatcroft, A. Robertson, A.R. Parsons, C.C. Wilson, Continuous crystallization of paracetamol (acetaminophen) form II: selective access to a metastable solid form, Cryst. Growth Des. 17 (2017) 2418–2427, https://doi.org/10.1021/acs.cgd.6b01831.

[20] A.F. Santos, L.S. Mendes, P. Alvarenga, L.M. Gando-Ferreira, M.J. Quina, Nutrient recovery via struvite precipitation from wastewater treatment plants: influence of operating parameters, coexisting ions, and seeding, Water 16 (2024) 1675, https://doi.org/10.3390/w16121675.

[21] K.S. Le Corre, E. Valsami-Jones, P. Hobbs, S.A. Parsons, Kinetics of struvite precipitation: effect of the magnesium dose on induction times and precipitation rates, Environ. Technol. 28 (2007) 1317–1324, https://doi.org/10.1080/09593332808618891.

[22] M. Fromberg, M. Pawlik, D.S. Mavinic, Induction time and zeta potential study of nucleating and growing struvite crystals for phosphorus recovery improvements within fluidized bed reactors, Powder Technol. 360 (2020) 715–730, https://doi.org/10.1016/j.powtec.2019.09.067.

[23] Md.M. Rahman, M.A.Mohd. Salleh, U. Rashid, A. Ahsan, M.M. Hossain, C.S. Ra, Production of slow release crystal fertilizer from wastewaters through struvite crystallization – a review, Arab. J. Chem. 7 (2014) 139–155, https://doi.org/10.1016/j.arabjc.2013.10.007.

[24] R. Boistelle, F. Abbona, Nucleation of struvite ($MgNH_4PO_4 \cdot 6H_2O$) single crystals and aggregates, Cryst. Res. Technol. 20 (1985) 133–140, https://doi.org/10.1002/crat.2170200204.

[25] L. Natividad-Marin, M.W. Burns, P. Schneider, A comparison of struvite precipitation thermodynamics and kinetics modelling techniques, Water Sci. Technol. 87 (2023) 1393–1422, https://doi.org/10.2166/wst.2023.061.

[26] E.V. Münch, K. Barr, Controlled struvite crystallisation for removing phosphorus from anaerobic digester sidestreams, Water Res. 35 (2001) 151–159, https://doi.org/10.1016/S0043-1354(00)00236-0.

[27] Y. Jaffer, T.A. Clark, P. Pearce, S.A. Parsons, Potential phosphorus recovery by struvite formation, Water Res. 36 (2002) 1834–1842, https://doi.org/10.1016/S0043-1354(01)00391-8.

[28] N.O. Nelson, R.L. Mikkelsen, D.L. Hesterberg, Struvite precipitation in anaerobic swine lagoon liquid: effect of pH and Mg:P ratio and determination of rate constant, Bioresour. Technol. 89 (2003) 229–236, https://doi.org/10.1016/S0960-8524(03)00076-2.

[29] J.W. Mullin, Crystallization, 4th ed, Butterworth-Heinemann, Oxford Boston, 2001.

[30] V.L. Snoeyink, D. Jenkins, Water Chemistry, Wiley, New York, 1980.

[31] M.I.H. Bhuiyan, D.S. Mavinic, R.D. Beckie, A solubility and thermodynamic study of struvite, Environ. Technol. 28 (2007) 1015–1026, https://doi.org/10.1080/09593332808618857.

[32] M.I.H. Bhuiyan, D.S. Mavinic, R.D. Beckie, Nucleation and growth kinetics of struvite in a fluidized bed reactor, J. Cryst. Growth 310 (2008) 1187–1194, https://doi.org/10.1016/j.jcrysgro.2007.12.054.

[33] N.C. Bouropoulos, P.G. Koutsoukos, Spontaneous precipitation of struvite from aqueous solutions, J. Cryst. Growth 213 (2000) 381–388, https://doi.org/10.1016/S0022-0248(00)00351-1.

[34] B. Tansel, G. Lunn, O. Monje, Struvite formation and decomposition characteristics for ammonia and phosphorus recovery: a review of magnesium-ammonia-phosphate interactions, Chemosphere 194 (2018) 504–514, https://doi.org/10.1016/j.chemosphere.2017.12.004.

[35] J. Borgerding, Phosphate deposits in digestion systems, J. Water Pollut. Control Fed. 44 (1972) 813–819.

[36] S.C. Galbraith, P.A. Schneider, A.E. Flood, Model-driven experimental evaluation of struvite nucleation, growth and aggregation kinetics, Water Res. 56 (2014) 122–132, https://doi.org/10.1016/j.watres.2014.03.002.

[37] C.M. Mehta, D.J. Batstone, Nucleation and growth kinetics of struvite crystallization, Water Res. 47 (2013) 2890–2900, https://doi.org/10.1016/j.watres.2013.03.007.

[38] G. Jia, H. Zhang, J. Krampe, T. Muster, B. Gao, N. Zhu, B. Jin, Applying a chemical equilibrium model for optimizing struvite precipitation for ammonium recovery from anaerobic digester effluent, J. Clean. Prod. 147 (2017) 297–305, https://doi.org/10.1016/j.jclepro.2017.01.116.

[39] S. Agrawal, J.S. Guest, R.D. Cusick, Elucidating the impacts of initial supersaturation and seed crystal loading on struvite precipitation kinetics, fines production, and crystal growth, Water Res. 132 (2018) 252–259, https://doi.org/10.1016/j.watres.2018.01.002.

[40] J.R. Burns, B. Finlayson, Solubility product of magnesium ammonium phosphate hexahydrate at various temperatures, J. Urol. 128 (1982) 426–428, https://doi.org/10.1016/S0022-5347(17)52952-3.

[41] M. Hanhoun, L. Montastruc, C. Azzaro-Pantel, B. Biscans, M. Frèche, L. Pibouleau, Temperature impact assessment on struvite solubility product: a thermodynamic modeling approach, Chem. Eng. J. 167 (2011) 50–58, https://doi.org/10.1016/j.cej.2010.12.001.

[42] Y.-H. Song, G.-L. Qiu, P. Yuan, X.-Y. Cui, J.-F. Peng, P. Zeng, L. Duan, L.-C. Xiang, F. Qian, Nutrients removal and recovery from anaerobically digested swine wastewater by struvite crystallization without chemical additions, J. Hazard. Mater. 190 (2011) 140–149, https://doi.org/10.1016/j.jhazmat.2011.03.015.

[43] E. Ariyanto, T.K. Sen, H.M. Ang, The influence of various physico-chemical process parameters on kinetics and growth mechanism of struvite crystallisation, Adv. Powder Technol. 25 (2014) 682–694, https://doi.org/10.1016/j.apt.2013.10.014.

[44] A.N. Kofina, P.G. Koutsoukos, Spontaneous precipitation of struvite from synthetic wastewater solutions, Cryst. Growth Des. 5 (2005) 489–496, https://doi.org/10.1021/cg049803e.

[45] D.S. Perwitasari, S. Muryanto, J. Jamari, A.P. Bayuseno, Kinetics and morphology analysis of struvite precipitated from aqueous solution under the influence of heavy metals: Cu2+, Pb2+, Zn2+, J. Environ. Chem. Eng. 6 (2018) 37–43, https://doi.org/10.1016/j.jece.2017.11.052.

[46] P. Zamora, T. Georgieva, I. Salcedo, N. Elzinga, P. Kuntke, C.J. Buisman, Long-term operation of a pilot-scale reactor for phosphorus recovery as struvite from source-

separated urine, J. Chem. Technol. Biotechnol. 92 (2017) 1035–1045, https://doi.org/10.1002/jctb.5079.
[47] C. Zhang, K. Xu, M. Zheng, J. Li, C. Wang, Factors affecting the crystal size of struvite-K formed in synthetic urine using a stirred reactor, Ind. Eng. Chem. Res. 57 (2018) 17301–17309, https://doi.org/10.1021/acs.iecr.8b03328.
[48] M. Quintana, E. Sánchez, M.F. Colmenarejo, J. Barrera, G. García, R. Borja, Kinetics of phosphorus removal and struvite formation by the utilization of by-product of magnesium oxide production, Chem. Eng. J. 111 (2005) 45–52, https://doi.org/10.1016/j.cej.2005.05.005.
[49] S. Ben Moussa, M.M. Tlili, N. Batis, M.B. Amor, Influence of tempereature on struvite precipitation by CO_2 -deagassing method, Cryst. Res. Technol. 46 (2011) 255–260, https://doi.org/10.1002/crat.201000571.
[50] M.S. Rahaman, N. Ellis, D.S. Mavinic, Effects of various process parameters on struvite precipitation kinetics and subsequent determination of rate constants, Water Sci. Technol. 57 (2008) 647–654, https://doi.org/10.2166/wst.2008.022.
[51] O. Fatibelo Filho, Equilíbrio Iônico: aplicações em Química Analítica, EdUFSCar, São Carlos, 2016.
[52] A. Triger, J.-S. Pic, C. Cabassud, Determination of struvite crystallization mechanisms in urine using turbidity measurement, Water Res. 46 (2012) 6084–6094, https://doi.org/10.1016/j.watres.2012.08.030.
[53] T.L. Brown, H.E. LeMAY Jr., B. Bursten, C. Murphy, P.M. Woodward, Chemistry: The Central Science, 12 th ed., Pearson Prentice Hall, USA, 2012.
[54] P. Van Rensburg, E.V. Musvoto, M.C. Wentzel, G.A. Ekama, Modelling multiple mineral precipitation in anaerobic digester liquor, Water Res. 37 (2003) 3087–3097, https://doi.org/10.1016/S0043-1354(03)00173-8.
[55] A.P. Bayuseno, D.S. Perwitasari, S. Muryanto, M. Tauviqirrahman, J. Jamari, Kinetics and morphological characteristics of struvite (MgNH4PO4.6H2O) under the influence of maleic acid, Heliyon 6 (2020) e03533, https://doi.org/10.1016/j.heliyon.2020.e03533.
[56] J. Prywer, A. Torzewska, T. Płociński, Unique surface and internal structure of struvite crystals formed by Proteus mirabilis, Urol. Res. 40 (2012) 699–707, https://doi.org/10.1007/s00240-012-0501-3.
[57] A. Siciliano, C. Limonti, G.M. Curcio, R. Molinari, Advances in struvite precipitation technologies for nutrients removal and recovery from aqueous waste and wastewater, Sustainability 12 (2020) 7538, https://doi.org/10.3390/su12187538.
[58] S. Shaddel, H. Bakhtiary-Davijany, C. Kabbe, F. Dadgar, S. Østerhus, Sustainable sewage sludge management: from current practices to emerging nutrient recovery technologies, Sustainability 11 (2019) 3435, https://doi.org/10.3390/su11123435.
[59] V. Babic-Ivancic, J. Kontrec, D. Kralj, L. Brecevic, Precipitation diagrams of struvite and dissolution kinetics of different struvite morphologies, in: Precipitation Diagrams of Struvite and Dissolution Kinetics of Different Struvite Morphologies 1, 2002, pp. 89–106.
[60] I. Enyemadze, F.W.Y. Momade, S. Oduro-Kwarteng, H. Essandoh, Phosphorus recovery by struvite precipitation: a review of the impact of calcium on struvite quality, J. Water Sanit. Hyg. Dev. 11 (2021) 706–718, https://doi.org/10.2166/washdev.2021.078.
[61] H.E. Swanson, M.C. Morris, E.H. Evans, L. Ulmer, Standard X-Ray Diffraction Powder Patterns, National Bureau of Standards Monograph, 1964.
[62] M.I.H. Bhuiyan, D.S. Mavinic, F.A. Koch, Thermal decomposition of struvite and its phase transition, Chemosphere 70 (2008) 1347–1356, https://doi.org/10.1016/j.chemosphere.2007.09.056.
[63] R.C.D.S. Meira, S.P.A.D. Paz, J.A.M. Corrêa, XRD-Rietveld analysis as a tool for monitoring struvite analog precipitation from wastewater: P, Mg, N and K recovery for fertilizer production, J. Mater. Res. Technol. 9 (2020) 15202–15213, https://doi.org/10.1016/j.jmrt.2020.10.082.
[64] T. Zhang, L. Ding, H. Ren, Pretreatment of ammonium removal from landfill leachate by chemical precipitation, J. Hazard. Mater. 166 (2009) 911–915, https://doi.org/10.1016/j.jhazmat.2008.11.101.
[65] K.N. Ohlinger, T.M. Young, E.D. Schroeder, Predicting struvite formation in digestion, Water Res. 32 (1998) 3607–3614, https://doi.org/10.1016/S0043-1354(98)00123-7.
[66] X. Lu, K. Shih, X. Li, G. Liu, E.Y. Zeng, F. Wang, Accuracy and application of quantitative X-ray diffraction on the precipitation of struvite product, Water Res. 90 (2016) 9–14, https://doi.org/10.1016/j.watres.2015.12.014.
[67] H. Li, Q.-Z. Yao, Z.-M. Dong, T.-L. Zhao, G.-T. Zhou, S.-Q. Fu, Controlled synthesis of struvite nanowires in synthetic wastewater, ACS Sustain. Chem. Eng. 7 (2019) 2035–2043, https://doi.org/10.1021/acssuschemeng.8b04393.
[68] European Parliament, Regulation (EU) 2019/1009 of the European Parliament and of the Council of 5 June 2019 laying down rules on the making available on the market of EU fertilising products and amending Regulations (EC) No 1069/2009 and (EC) No 1107/2009 and repealing Regulation (EC) No 2003/2003. https://eur-lex.europa.eu/eli/reg/2019/1009/oj/eng, 2019.